(Received 23 January 2026, Accepted 5 March 2026, Scheduled 25 March 2026)

Isolation Enhancement in Polyimide-Based MIMO Antennas Using Slot-Based Metamaterial Defected Ground Structures and a Stub-Loaded Decoupling Network

Ahmed J. A. Al-Gburi[1,*], Kudumu V. Prasad[2], Venkata N. K. R. Devana[3], Ghali S. Rao[4], Ammar Armghan[5], and Anuar M. Kassim[6,7,*]

[1]*Strategic Research Institute (SRI), Asia Pacific University Jalan Teknologi 5, Taman Teknologi Malaysia, 57000 Kuala Lumpur, Malaysia*
[2]*ECE, Vasireddy Venkatadri International Technological University, Nambur, Guntur, Andhra Pradesh, India*
[3]*ECE Department, Aditya University, Surampalem, Andhra Pradesh, India*
[4]*ECE Department, ALCRC Lab, KLEF, Guntur, India*
[5]*Department of Electrical Engineering, College of Engineering, Jouf University, 72388 Sakaka, Saudi Arabia*
[6]*Center of Robotics and Industrial Automation, Faculty of Technology and Electrical Engineering Universiti Teknikal Malaysia Melaka, Hang Tuah Jaya, 76100 Durian Tunggal, Melaka, Malaysia*
[7]*IngeniousCity Engineering Solutions (ICES), Sdn. Bhd. No 79-1, Jalan Satu Krubong Taman Satu Krubong, 75250 Krubong, Melaka, Malaysia*

ABSTRACT: This research article presents a low-profile ultra-wideband (UWB) multiple-input multiple-output (MIMO) antenna with enhanced isolation and wideband performance, employing polyimide as the substrate. The suggested configuration consists of two symmetric radiating elements incorporating rectangular and circular slots within a compact footprint of $36 \times 21.1 \times 0.1\,\text{mm}^3$. To effectively suppress mutual coupling, a slot-based metamaterial-inspired defected ground structure (DGS) with a meandered profile is introduced between the antenna elements. In addition, inverted U-shaped stubs and optimally placed slots are integrated to form a stub-loaded decoupling network, further improving inter-element isolation across the UWB spectrum. The antenna exhibits resonant modes at 4.16 GHz (WLAN), 5.49 GHz (IoT and smart home applications), 7.54 GHz (satellite and point-to-point communications), and 11.61 GHz (high-resolution imaging and sensing), covering the 4–12 GHz frequency range. Predicted and tested outcomes present good agreement, with key MIMO performance parameters achieving Channel Capacity Loss (CCL) below 0.4 bits/s/Hz, diversity gain (DG) above 9.9 dB, Envelope Correlation Coefficient (ECC) below 0.005, and Total Active Reflection Coefficient (TARC) less than -10 dB. Owing to its compact size, wideband operation, and high isolation characteristics, the suggested antenna is a strong candidate for wireless area networks and emerging IoT-based sensing applications.

1. INTRODUCTION

UWB antennas exhibit more effective channel capacity, envelope correlation, and diversity gain than traditional narrowband antennas [1]. To address these issues and improve the communication performance of wearable devices, the adoption of MIMO antenna technology has become a focal point of research and development [2]. In [2], a MIMO wearable system is introduced, featuring four coplanar waveguide-fed hexagonal-shaped monopole radiators designed to operate within the 4.4–5 GHz range. This system is developed on a polyimide material with dimensions of $1.33\lambda_0 \times 1.03\lambda_0$. By arranging the four radiating elements orthogonally, the system achieves enhanced isolation exceeding 17 dB. Additionally, the use of a flexible substrate allows for conformability, which is validated through bending analysis. In [3], a single-layered MIMO design with planar-patterned metamaterial structure is presented for mm-wave applications. A split-square and hexagonal metamaterial unit cell is considered and analyzed. With a 4 mm element spacing, the design ensures improved isolation and exhibits strong MIMO performance. In [4], a dual-band, 4-port MIMO design for mm-wave 5G wearable applications on a Rogers 3003 material is proposed. Each element features a composite circular-elliptical structure with a thin strip and tapered feed line. Bending and Specific Absorption Rate (SAR) evaluations confirm its safety within acceptable limits. In [5], a four-element MIMO antenna for the WLAN is proposed, with a defective ground structure (DGS) designed using characteristic mode analysis to enhance performance. In [6], a circularly slotted fractal super wide-band (CSF-SWB) antenna on a $24 \times 30\,\text{mm}^2$ FR-4 substrate is proposed for WiFi-5, WiMAX, WLAN, 5G, UWB, and Ku-Ka band applications. Introducing DGS provides a 2.99–95.82 GHz bandwidth, making it ideal for super wideband applications.

In [7], a novel foot-shaped Elliptically Embedded Patch (EEP) with four-band rejection is presented. It uses embedded ellipses, a defective rectangular ground structure (DRGS),

* Corresponding authors: Ahmed Jamal Abdullah Al-Gburi (ahmedjamal@ieee.org); Anuar Mohamed Kassim (anuar@utem.edu.my).

and four $\lambda/2$ inverted U-slots for band stops, verified by Characteristic Mode Analysis (CMA). A new $24 \times 28\,\text{mm}^2$ elliptically slotted antenna (ESA) on an FR-4 substrate with beveled DGS offers bandwidth from 3.42 to 11.79 GHz [8]. Two notched bands are created by etching an S-shaped slot in the feed line and an irregular C-shaped parasitic stub above the DGS for UWB. An octagonal MIMO-UWB antenna features parasitic stubs to decrease coupling between MIMO elements on a cost-effective $40 \times 23\,\text{mm}^2$ FR4 substrate [9]. The antenna covers UWB, extended UWB, and Ku-band frequencies from 3.28 to 17.8 GHz for global applications. Critical performance parameters with 0.003 ECC and 9.997 dB DG are evaluated. In [10], a compact anti-parallel millimeter-wave UWB-MIMO antenna achieves 65 dB isolation by anti-parallel design and proper inter-element spacing. The miniatured dimensions, $6 \times 17.37\,\text{mm}^2$, with DGS increase isolation by 20 dB. In [11], we provide a $20 \times 32 \times 1.62\,\text{mm}^3$ compact circular high-gain MIMO antenna with a fractal DGS on an FR4 substrate for satellite downlink applications. Over the operating frequency range from 15.946 to 17.973 GHz, the antenna elements have 16 mm spacing, and the antenna achieves isolation above 15 dB. Its gain is 6.25 dBi and reflection coefficient -43.82 dB. In [12], a $40 \times 50\,\text{mm}^2$ lightweight MIMO printed UWB antenna with a quarter-circular radiating patch is proposed with over -15 dB isolation for the frequency 2.67–14 GHz. Two identical radiating components spaced at 4 mm and a diamond-shaped slot enable dual-band wireless communication at 8.2 GHz and 14.0 GHz in the tiny inset-fed rectangular MIMO patch antenna [13]. Diamond slots from rectangular radiating patches and ground plane circular slots reduce reciprocal coupling and promote diversity. A four-port circular monopole with split-ring slots MIMO antenna with reconfigurable UWB notches and a U-shaped feed line slot provides band notches at 4.3 GHz, 6.8 GHz, and 8.3 GHz. To isolate orthogonal MIMO portions, a decoupling structure is placed between them. A tiny, crescent-shaped split ring within a circular monopole and a rectangular helix slot along the feed line generate a wideband MIMO antenna with quadruple notches for 3 to 18 GHz [14]. In [15], reduced coupling is achieved using orthogonal MIMO components. The 3 GHz element is tiny ($0.28\lambda \times 0.22\lambda \times 0.016\lambda$), making it suited for portable electronics. The ultra-wide band UWB-MIMO antenna proposed in [16] is only $42 \times 30 \times 1.6\,\text{mm}^3$. Two rectangular radiating devices with small holes provide 3.1–10.6 GHz UWB bandwidth. An elliptical partial ground decoupling structure improves UWB spectrum isolation > 15 dB. Simulations and observations of all diving parameters are allowed. In [17], a $50 \times 25\,\text{mm}^2$ FR4 MIMO antenna with two radiators and four T-shaped slots on all sides of the radiator is analyzed. Mutual coupling (MC) and impedance bandwidth (IBW) are reduced by a ground stub, which is T-shaped, and a slot. On the UWB spectrum, this design allows WiMAX, WLAN, X-band SATCOM, Radar, and commercial WLAN. An innovative 2-element MIMO antenna with slotted elements and M-shaped DGS reduces MC on $50 \times 36\,\text{mm}^2$ FR4 [18]. M-shaped DGS and slotted element minimize the MC. The suggested structure resonates at 3.5 GHz, 5.9 GHz, 7.9 GHz, and 9.3 GHz in the UWB. In [19, 20], a unique planar construction, including varied 2-port UWB antennas with enhanced isolation and a common ground, is proposed utilizing an innovative slot loading technique. An elongated slot featuring an end-fire pattern is inscribed in the central upper section of a coplanar waveguide (CPW) in one design, and a decoupling structure is implemented on the ground in another structure. In [21], opposite-faced semi-circular monopoles form a miniaturized two-port UWB-MIMO antenna. The proposed radiator is optimized at $20 \times 20\,\text{mm}^2$. The orthogonal orientation of radiating elements provides low ECC and good pattern diversity. In [22], an array of three quad-G shaped metamaterial structures was used between the elements to enhance the bandwidth in the lower frequency band of UWB application and reduce the mutual coupling. This proposed MIMO antenna operates over a bandwidth of 8 GHz from 4 GHz to 12 GHz with the mutual coupling between elements < -19.0 dB with an inter-element separation of $\lambda/6$ mm, and the optimized dimensions are $0.34\lambda \times 0.22\lambda \times 0.021\lambda$ for a wavelength λ, calculated at 4 GHz. In [23], a compact MIMO antenna is proposed with high seclusion and band-reject qualities for UWB applications with optimized dimensions of $18 \times 36 \times 1.6\,\text{mm}^3$. It comprises of two monopole elliptical radiating elements, and to enhance the isolation between elements, a T-moulded stub is extruded in the ground plane. To achieve band-indented function for a wireless local area network (LAN), a dumbbell (I) moulded stub is extruded. The realized gain of the proposed design is above 2.8 dBi, with ECC < 0.1, TARC < -10 dB, MEG < -3 dB, CCL < 0.29 bps/Hz, and DG > 9.95 dB, which shows high diversity performance. In [24], a comprehensive review is presented that covers various techniques, their operating principles, and an analysis of electromagnetic (EM) isolation performance supported by experimental results obtained from fabricated prototypes, thereby validating the effectiveness of the proposed isolation methods. In [25], several design approaches — including metamaterials, metasurfaces, frequency selective surfaces (FSSs), defected ground structures (DGSs), parasitic elements, and orthogonal configurations — are discussed in detail along with their performance in enhancing gain and isolation. The work proposes a novel MIMO antenna structure that achieves improved gain and isolation by integrating two techniques, namely intelligent reflecting surfaces (IRSs) and reconfigurable intelligent surfaces (RISs). The proposed antenna is suitable for applications such as WLAN, Wi-Fi, WiMAX, LTE, ISM, Bluetooth, radar, satellite communication, 5G, and beyond-5G systems. In [26], a two-element antenna operating at 5.8 GHz is presented. To improve the isolation between the elements, a zigzag groove is introduced between them, forming a DGS that reduces mutual coupling by 28.8 dB. The ECC is maintained below 0.02, demonstrating its suitability for narrowband IoT applications. In [27], a compact printed omni-

directional metamaterial-inspired antenna with dimensions of 10.3 mm × 10.3 mm × 0.0787 mm was developed for air pollution monitoring in the Ka-band (26.5–40 GHz). The antenna exhibits dual-band operation at 27.49–29.74 GHz and 33.0–34.34 GHz, achieving gain levels ranging from 3.26 to 5.50 dBi in the first band and 5.09 to 6.52 dBi in the second band. The proposed sensor can be adapted for detecting metallic pollu-

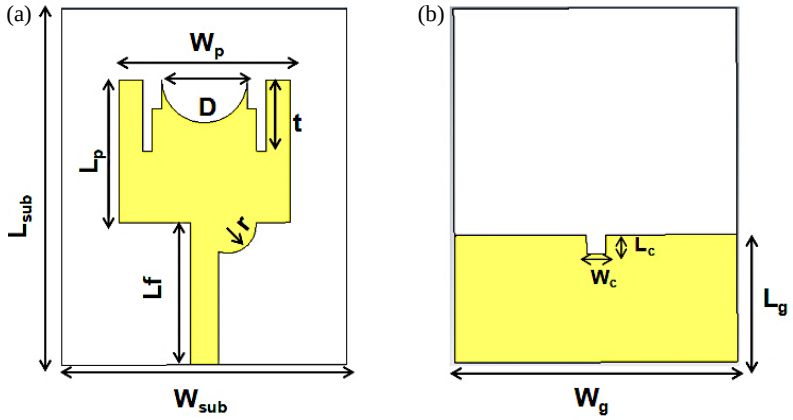

FIGURE 1. Single element, (a) patch, and (b) ground views.

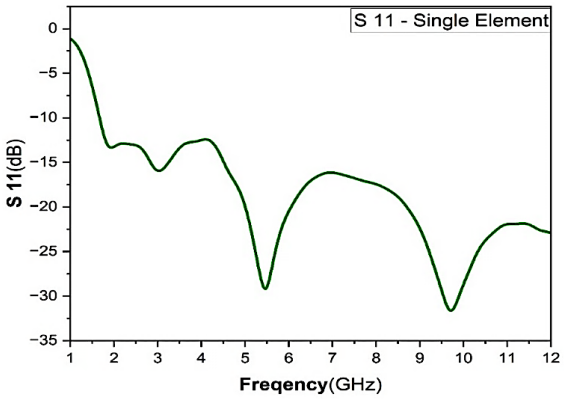

FIGURE 2. S_{11} plot of a single port.

tants in water and other fluid-based mediums, and may also be utilized in long-range communication repeaters and 5G energy-harvesting applications.

This article presents a miniaturized dual-element MIMO antenna configuration, in which each radiating element incorporates rectangular and circular slots within the patch geometry to achieve broadband performance. To effectively suppress the mutual coupling between the antenna elements, a stub-loaded decoupling network is introduced in combination with a DGS integrated into the ground plane. The novelty is that the proposed design utilizes a compact dual-element configuration that incorporates simple, rounded corner, rectangle-shaped radiators, DGS, and decoupling structures within a flexible substrate. This approach distinguishes it from conventional designs, where isolation structures and metamaterial loading are typically implemented as separate structures. The DGS beneath the radiators is not a generic slot structure but a purposefully arranged set of etched sections positioned to suppress surface current propagation between the ports. This produces isolation enhancement without requiring large inter-element spacing or neutralization lines. The antenna is realized on a polyimide substrate with overall dimensions of $36 \times 21.1 \times 0.1\,\text{mm}^3$, enabling a low-profile and lightweight implementation suitable for compact wireless devices. The proposed MIMO system demonstrates UWB operation, with the reflection and transmission coefficients satisfying standard performance criteria, namely $|S_{11}|$ below $-10\,\text{dB}$ and $|S_{12}|$ below $-15\,\text{dB}$ across the targeted frequency range.

2. ANTENNA DESIGN

2.1. Single Element Design

Figure 1 illustrates the geometry of a radiating element of the proposed antenna with dimensions of $20 \times 21.1 \times 0.1\,\text{mm}^3$, and its simulated S_{11} is presented in Figure 2. The design features a patch with a circular slot and an asymmetrical U-shaped slot at the edges within the UWB range. A semi-circular protrusion is introduced with radius 'r' at the feedline to enhance the bandwidth of a single element. The optimized dimensions of the single element are shown in Table 1.

TABLE 1. Specifications of single element.

Variables	Optimized values (mm)	Variables	Optimized values (mm)
L_{sub}	21.1	t	4
W_{sub}	20	D_1	5.4
L_p	10.8	W_g	20
W_p	8.43	L_g	8.4
L_f	8.43	W_c	2
r	2.95	L_c	2

2.2. Proposed Polyimide-Based MIMO Design

The two-element MIMO antenna, illustrated in Figure 3, is simulated and fabricated on a flexible polyimide substrate with $\varepsilon_r = 3.5$, $\tan = 0.001$, and overall dimensions of $W_s \times L_s$ ($36 \times 21.1\,\text{mm}^2$). The inter-element edge-to-edge spacing is maintained at 6 mm to achieve compactness while minimizing mutual coupling [28]. To further improve isolation performance, a meandered C-shaped DGS is incorporated in the ground plane, as depicted in Figure 3. Table 2 depicts the dimensions of modelled MIMO.

The antenna design incorporates a step-shaped truncation combined with a semi-circular slot. The semi-circular slot alters the effective electrical length, creates additional current

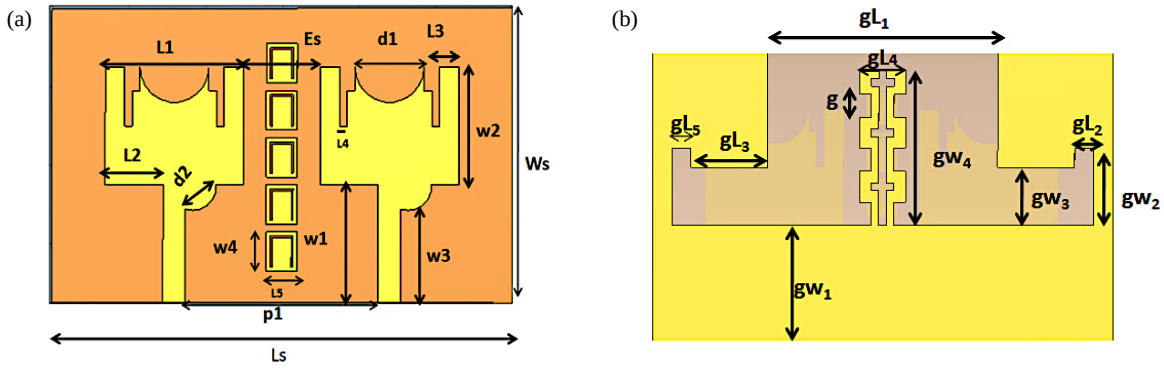

FIGURE 3. Proposed antenna design, (a) patch perspective, (b) ground perspective.

TABLE 2. Specifications of the MIMO design.

Variables	Optimized values (mm)	Variables	Optimized values (mm)	Variables	Optimized values (mm)
L_1	10.8	d_1	5.4	g_{L2}	1.5
L_2	4.5	d_2	2.95	g_{L3}	6
L_3	2.1	g_{w2}	5.6	g_{L4}	3.6
L_s	36	g_{w4}	11.25	gL_5	1.5
w_1	8.43	L_4	0.6	g	1.6
w_2	8.43	p_1	15.06	g_{w1}	8.4
w_3	6.7	L_5	2.4	g_{w3}	4.2
w_s	21.1	w_4	2.8	–	–
E_s	6	g_{L1}	18	–	–

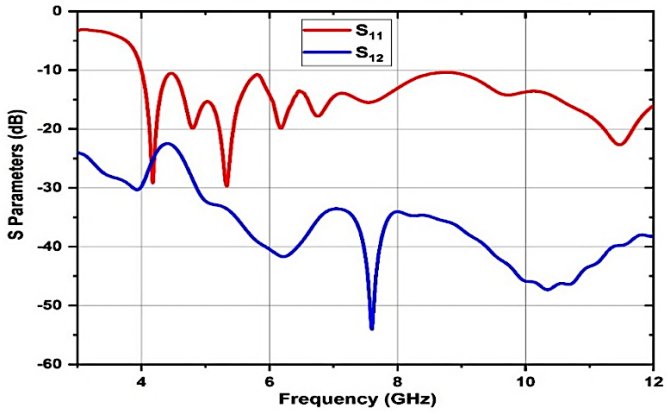

FIGURE 4. Simulated S_{11} and S_{12}.

paths to widen the bandwidth, improves impedance matching, and enables a more compact MIMO design. The S_{11} and S_{12} parameters of the proposed design are simulated, using High Frequency Structure Simulator (HFSS), and shown in Figure 4. To enhance isolation and suppress surface waves, a DGS is implemented beneath the substrate. Additionally, a rectangular slot is added to the partial ground to widen the operational bandwidth. The design features a patch with a circular slot and an asymmetrical U-shaped slot at the edges of the radiating element. The progress of the MIMO antenna is introduced in Figure 5.

Figure 5 demonstrates the step-by-step evolution of a MIMO design incorporating various modifications. Figure 5(a) shows the simple monopole design. Figures 5(b)–(d) demonstrate the gradual implementation of rectangular slots for impedance matching and bandwidth enhancement. Figure 5(e) introduces semi-circular slots for further performance optimization. Figures 5(f) and 5(g) depict the final proposed design with decoupling elements and DGS to improve isolation between the elements. Figure 6 illustrates the S_{11} performance for each iteration depicted in Figure 5 over a frequency of 3 to 12 GHz. The different iterations in the antenna structure result in improved impedance matching and wider bandwidth, as demonstrated by deeper and wider S_{11} below -10 dB in the final design.

2.3. Parametric Analysis

2.3.1. Variation of the Parameter d_1

The parametric study with variation in the parameter d_1 demonstrates that both impedance matching and isolation characteristics are strongly influenced by this parameter, as depicted in Figures 7 and 8. As observed in the S_{11} response in Figure 7, multiple resonances are excited between 4 GHz and 12 GHz, with the optimized case of $d_1 = 5.4$ mm exhibiting deeper and more stable return loss values, reaching below 20 dB around 5 GHz. In contrast, other values of d_1 (3.4 mm, 4.4 mm, and 5 mm) result in relatively shallow dips, indicat-

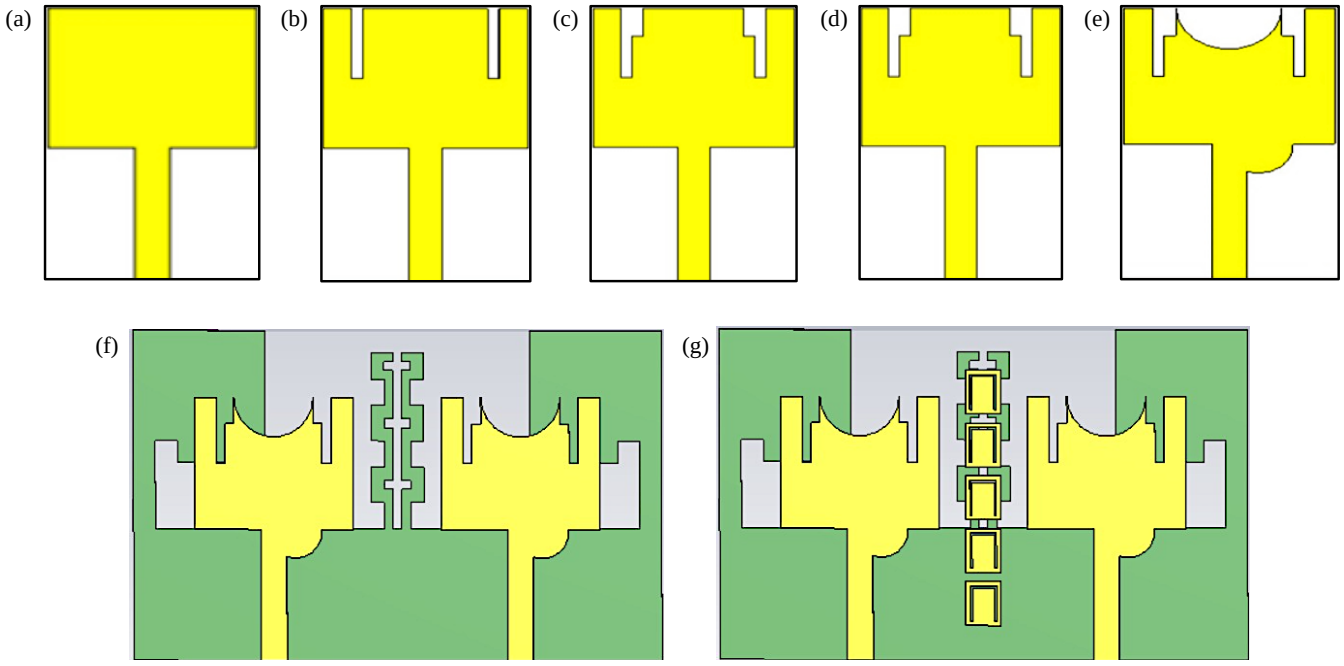

FIGURE 5. Evolution stages of the proposed design.

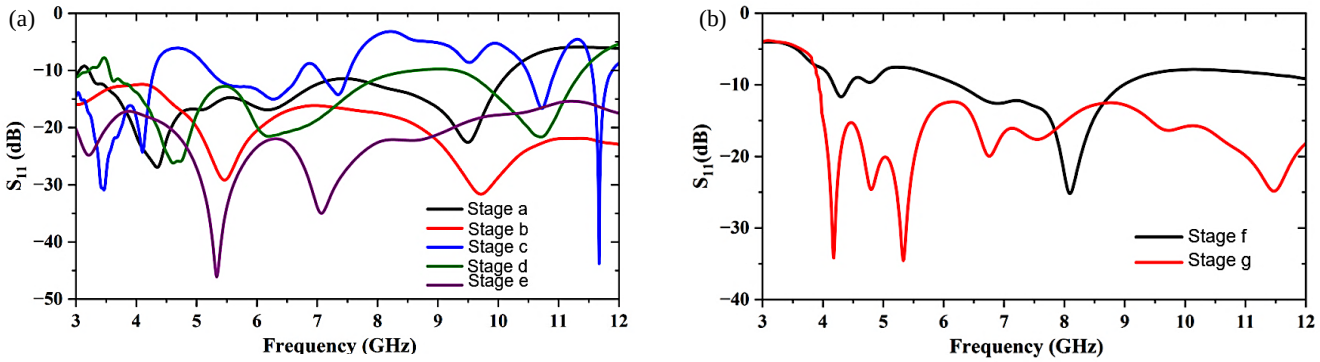

FIGURE 6. S_{11} plot of MIMO design in different evolution stages.

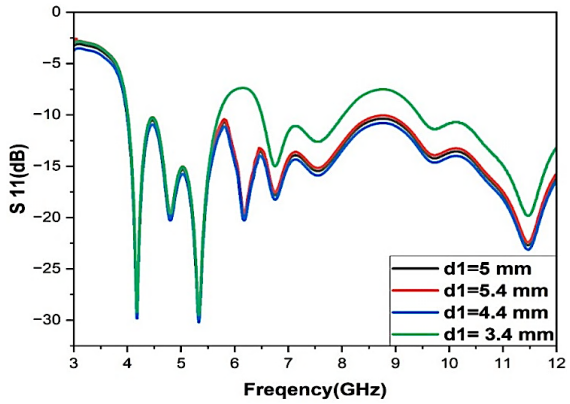

FIGURE 7. Performance of S_{11} for the variation of parameter d_1.

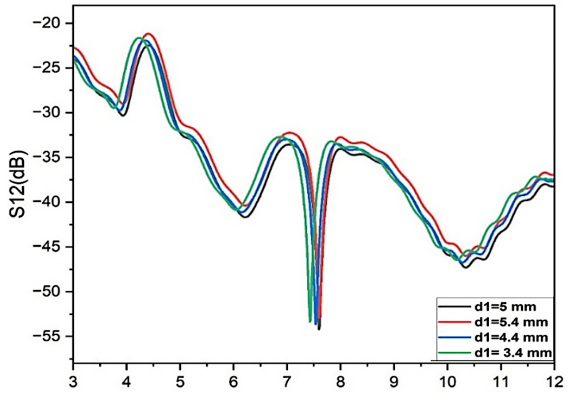

FIGURE 8. Performance of S_{12} for the variation of parameter d_1.

ing degraded impedance matching and narrower effective bandwidth. Similarly, the S_{12} characteristics confirm that isolation remains below 20 dB across the band, while the optimized case achieves superior coupling suppression, with isolation levels from -23 dB to -54 dB across the band. These results validate that the chosen value of $d_1 = 5.4$ mm offers the best trade-off,

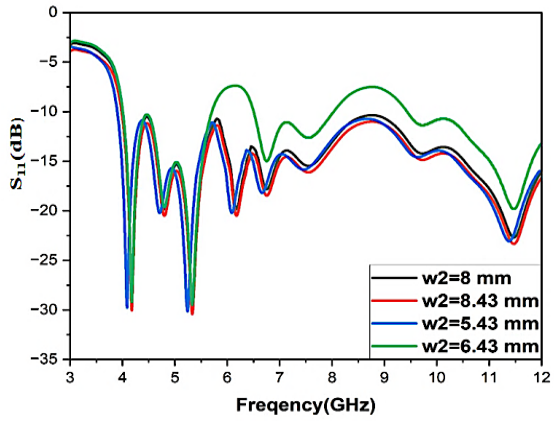

FIGURE 9. Performance of S_{11} for the variation of parameter W_2.

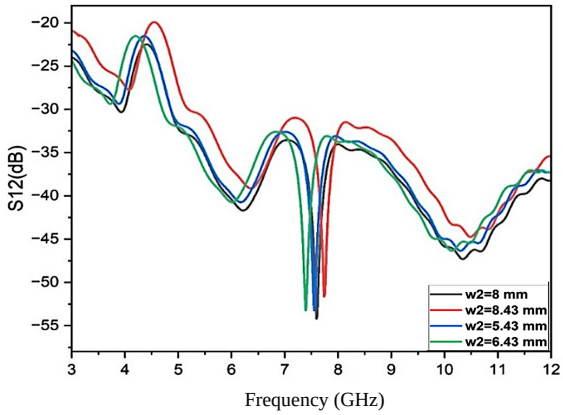

FIGURE 10. Performance of S_{12} for the variation of parameter W_2.

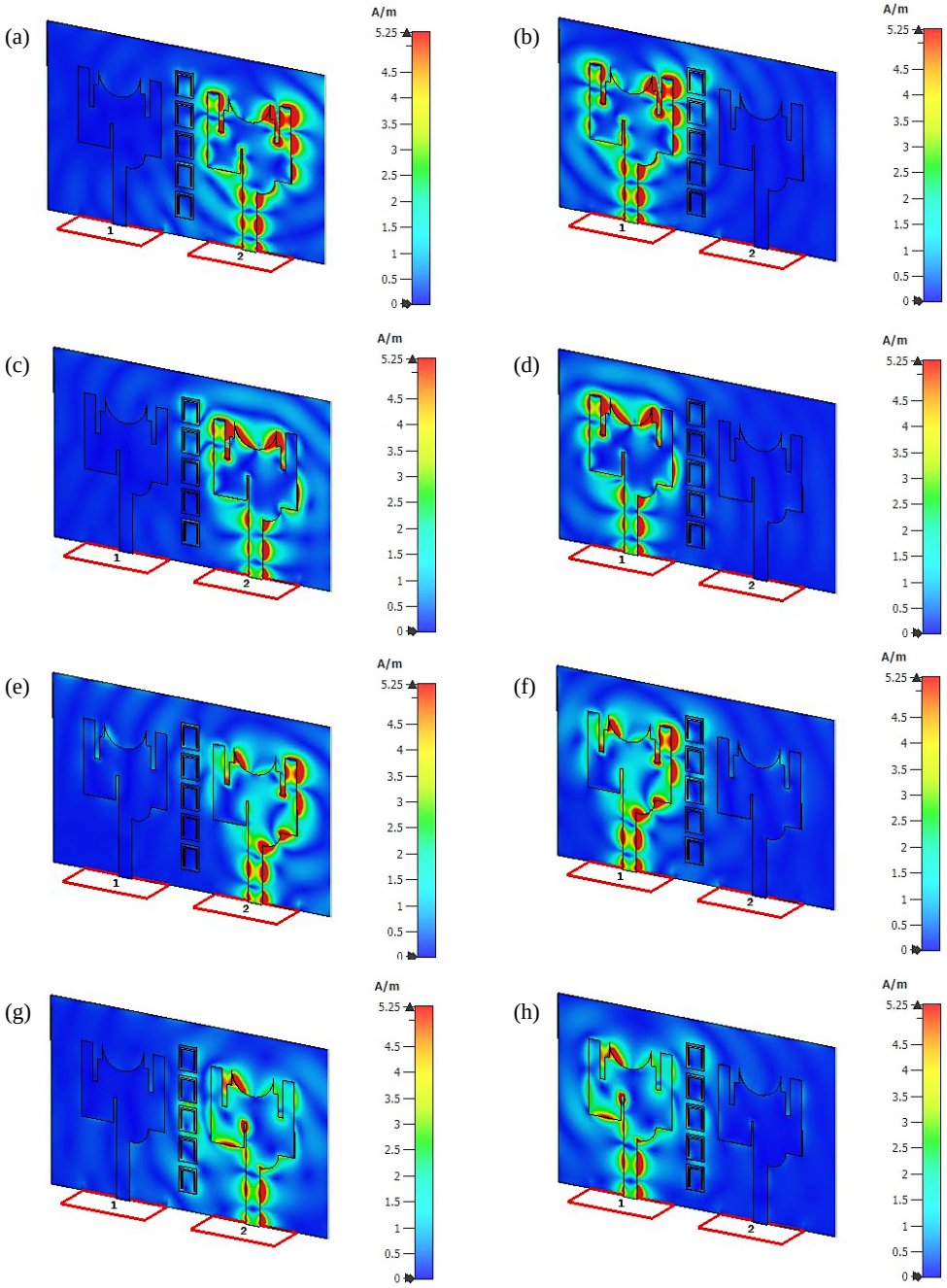

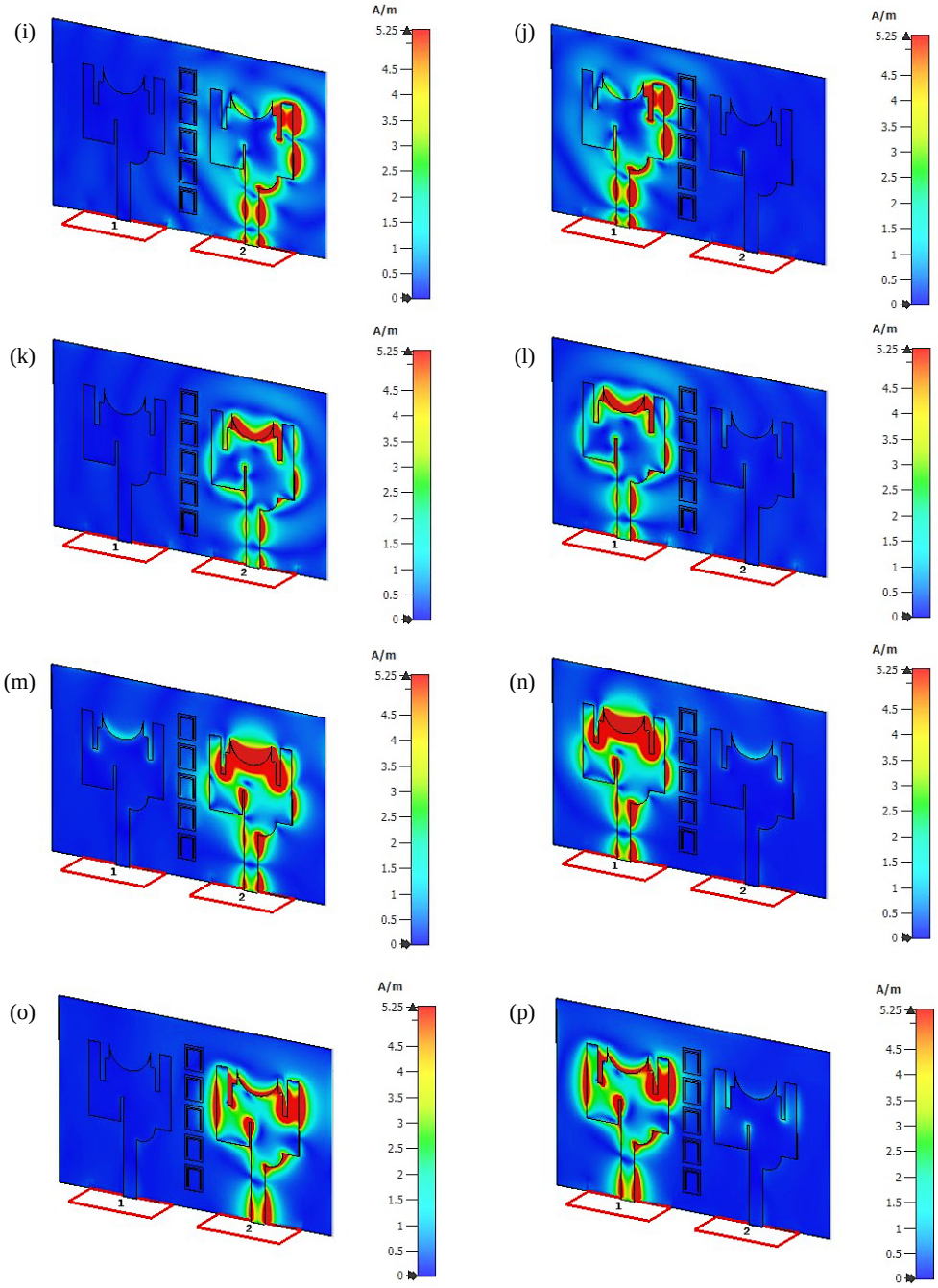

FIGURE 11. Surface current distributions of the proposed antenna at different operating frequencies for port 2 and port 1 (a) & (b) 4.16 GHz, (c) & (d) 5.49 GHz, (e) & (f) 7.54 GHz, (g) & (h) 8.4 GHz, (i) & (j) 9.08 GHz, (k) & (l) 10.15 GHz, (m) & (n) 11.02 GHz, and (o) & (p) 11.61 GHz.

ensuring wideband impedance stability along with enhanced inter-element isolation, thereby confirming its suitability for the proposed antenna configuration.

2.3.2. Variation of the Parameter W_2

The parametric evaluation, with variation in W_2, highlights its influence on both isolation characteristics and impedance matching across the 3–12 GHz band, as shown in Figures 9 and 10, respectively. From the S_{11} response, it is observed that all cases produce multiple resonances; however, the optimized width of $W_2 = 8.43$ mm provides the most consistent impedance matching with well-defined S_{11} dips below 20 dB at several resonant frequencies, particularly around 4 GHz, 5.1 GHz, and 11.2 GHz. In contrast, smaller widths, such as 5.43 mm and 6.43 mm, result in relatively shallower resonances, while larger widths, such as 8 mm, slightly distort the bandwidth uniformity. This indicates that the optimized W_2 value ensures improved impedance bandwidth and stable multi-resonant behavior. The isolation characteristics (S_{12}) further confirm this trend, where $W_2 = 8.43$ mm achieves enhanced coupling suppression with isolation levels approaching -55 dB in the mid-frequency range of 7–8 GHz, compared to weaker isolation (-20 dB to -42 dB) for the other parameter

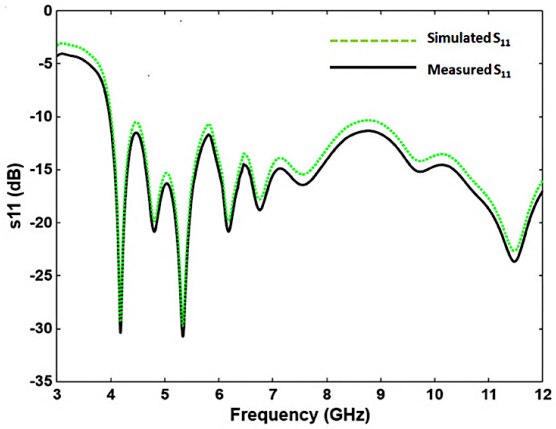

FIGURE 12. Predicted and tested S_{11}.

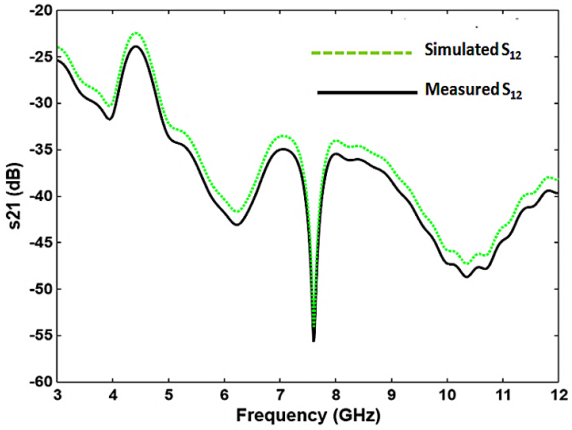

FIGURE 13. Predicted and measured S_{12}.

values. At higher frequencies ($\sim$ 10–11 GHz), the performance converges across all cases, and yet the optimized design maintains a superior margin of isolation. These results verify that $W_2 = 8.43$ mm offers the best trade-off between achieving strong inter-element isolation and wideband impedance matching, validating its selection as the proposed parameter for the antenna.

2.4. Surface Current Distributions and Radiation Pattern

The surface current distribution of the design is depicted in Figure 11. As apparent from Figure 11, the meander line shaped DGS varies the current distribution and thereby minimizes the MC between two elements [29]. The surface current distributions are simulated at 4.16 GHz (WLAN), 5.49 GHz (IoT and smart home devices), 7.54 GHz (Satellite and Point-to-Point Communications), 8.4 GHz (SatCom), 9.08 GHz (Remote Sensing), 10.15 GHz (Defense and military), 11.02 GHz (High-Speed Wireless LAN and Fixed Wireless Access), and 11.61 GHz (High-resolution imaging and sensing) for both ports of the design. As the elements are separated by several decoupling structures on the ground to reduce MC, the distribution is analyzed for different specific frequency applications.

3. RESULT ANALYSIS WITH DISCUSSION

The antenna is printed on a polyimide with a thickness of 0.1 mm using standard printed circuit board (PCB) fabrication techniques. Key parameters, including S_{11}, S_{21}, pattern, and gain, are analyzed in an anechoic chamber and compared with simulated results. The S_{11} of the proposed design was evaluated employing an Anritsu vector network analyzer (VNA), confirming a bandwidth of 3.1–12 GHz with S_{11} below 10 dB. The proposed design was tested and fabricated using a VNA [30]. Figures 12 and 13 present a comparison between the simulated and outcomes obtained from measurements for S_{11} and S_{21}, respectively. The simulated and tested S_{12} values are shown in Figure 13, demonstrating MC below 15 dB across the 3.1–12 GHz bandwidth. The maximum isolation of 56.4 dB is attained at 7.62 GHz. Throughout the entire operating bandwidth, the S_{12} remains consistently below 22.4 dB, indicating excellent isolation performance.

Figure 14 illustrates the E-plane and H-plane patterns, comparing simulated and measured results at 4.16 GHz, 5.49 GHz, and 7.54 GHz. The red solid line signifies the simulated co-polarization, while the blue dashed line illustrates the measured co-polarization. The magenta solid line corresponds to the simulated cross-polarization, and the black dashed line indicates the measured cross-polarization. The antenna's performance is confirmed through the agreement between simulated and results obtained from measurements, demonstrating strong co-polarization characteristics and effectively reduced cross-polarization levels [31]. Figure 15 illustrates the fabricated prototype of the antenna, showing (a) front view, (b) back view, (c) the anechoic chamber setup for measurement, and (d) the VNA configuration used for experimental validation.

The antenna is modeled using a multi-branch parallel RLC circuit, in which each RLC network represents the main patch, slots, and DGS, indicating individual resonant modes arising from the current and field distributions on the structure [32]. The equivalent circuit is shown in Figure 16. The resistive components correspond to radiation and loss mechanisms. From Figure 17, it can be observed that the DGS-only configuration provides isolation in the range of approximately -23 to -42 dB, while the stub-loaded network alone achieves about -23 to -53 dB with localized improvement near its resonance. When the two techniques are combined, the isolation is significantly enhanced to nearly -45 to -60 dB across the operating band, corresponding to an additional improvement of approximately 15–20 dB over the DGS-only case and 10–15 dB over the stub-only configuration. The good agreement between circuit response and EM results confirms that the antenna operates as a multi-resonant system, validating the proposed design mechanism.

4. MIMO PERFORMANCE ANALYSIS

The MIMO system performance is strongly influenced by the design of the individual elements as well as their mutual coupling within the array configuration. To comprehensively evaluate the effectiveness of a MIMO antenna system, several key

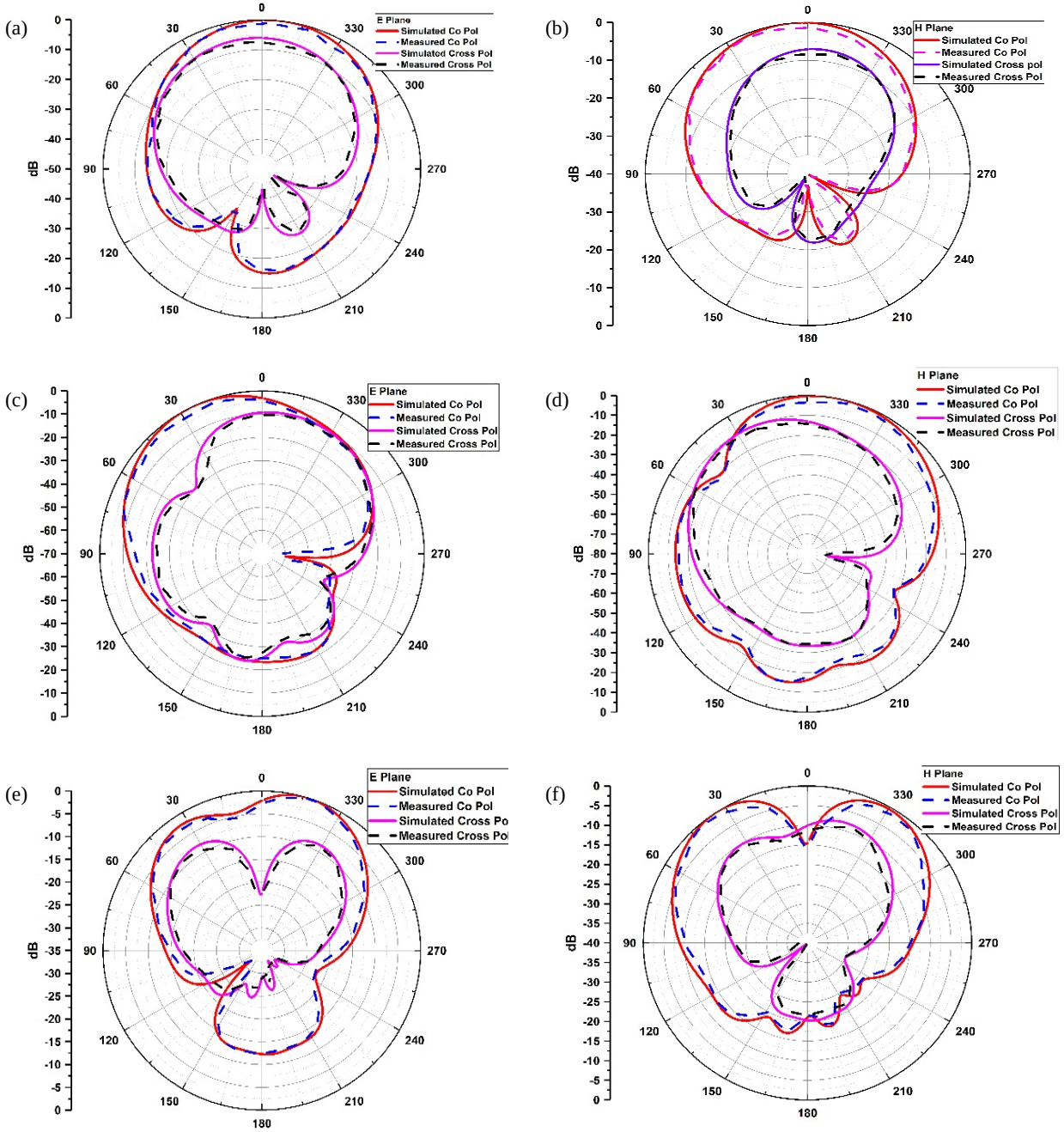

FIGURE 14. Predicted and tested co-polarized and cross-polarized radiation characteristics in the E- and H-planes at the resonant frequencies of 4.16 GHz, 5.49 GHz, and 7.54 GHz.

diversity and correlation parameters are considered, including ECC, DG, TARC, and CCL. These metrics collectively provide a better understanding w.r.t the isolation, radiation diversity, impedance matching, and information theoretic capacity of the MIMO system, thereby ensuring reliable performance in multipath wireless environments.

4.1. ECC

ECC measures the correlation between patterns of the elements in a MIMO system. Low values of ECC signify better isolation and diversity between the elements, which enhances the system's capability to combat multipath interference. The ideal value of ECC is < 0.5, and for optimal performance, ECC should ideally be below 0.01. ECC can be calculated using the S-parameter method or the 3D radiation method. A low ECC ensures uncorrelated signal paths, thus improving the system's overall capacity. ECC in terms of S-parameters is expressed in Equation (1) [33]:

$$ECC = \frac{\left|S_{11}^{*}S_{12}+S_{21}^{*}S_{22}\right|^{2}}{\left(1-\left|S_{11}\right|^{2}-\left|S_{21}\right|^{2}\right)\left(1-\left|S_{22}\right|^{2}-\left|S_{12}\right|^{2}\right)} \quad (1)$$

The measured and simulated ECCs are indicated in Figure 18 and maintain a value of < 0.0001 over the entire UWB range, as shown in Figure 18.

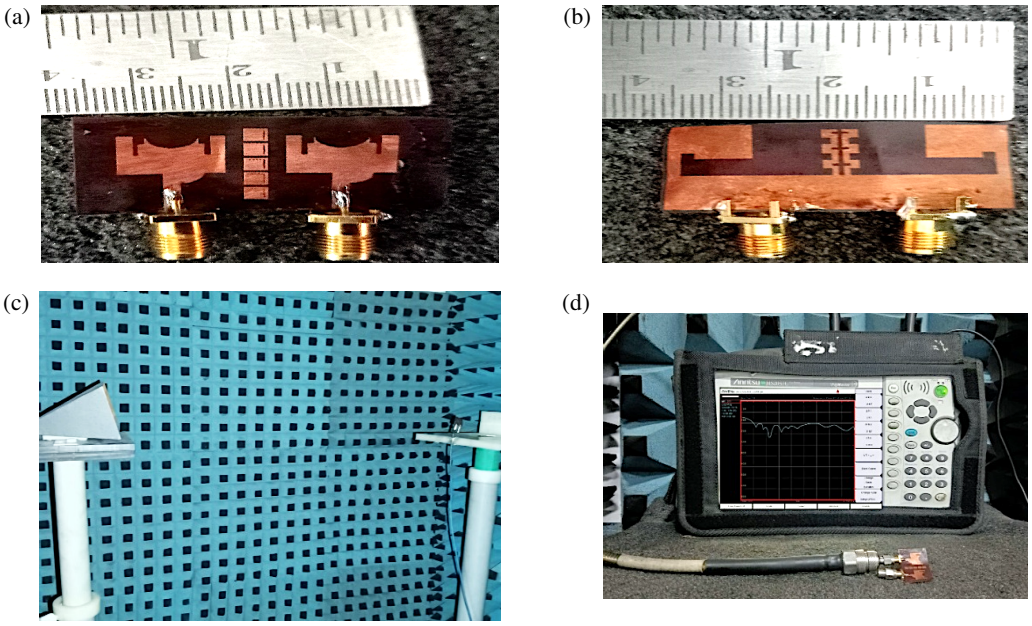

FIGURE 15. Fabricated model with metamaterial: (a) MIMO patch view; (b) MIMO ground view; (c) setup for measurement; and (d) VNA setup.

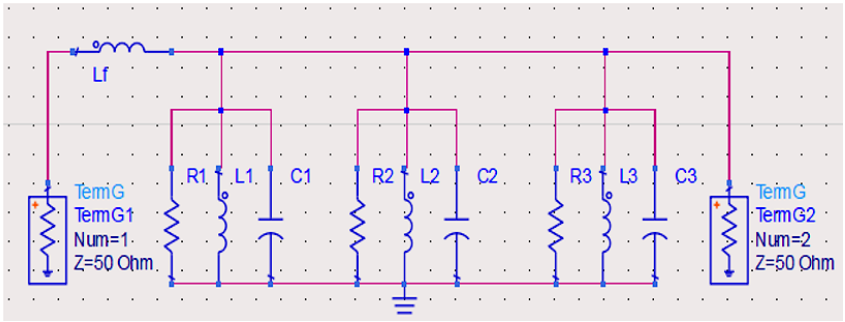

FIGURE 16. Equivalent circuit representation of the proposed design.

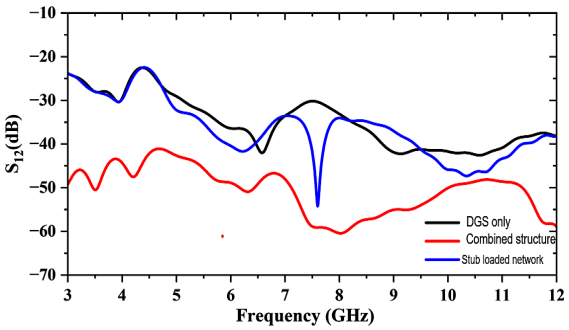

FIGURE 17. S_{12} for the proposed design with DGS only, stub-loaded network, and the combined structure.

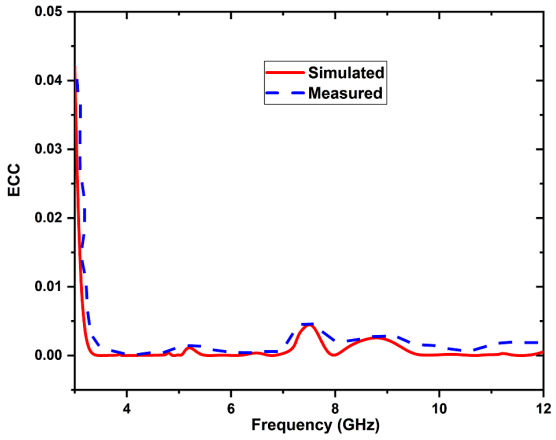

FIGURE 18. ECC of the proposed model.

4.2. DG

DG measures the improvement in signal quality due to diversity techniques. It is directly related to ECC and is a representation of how well the antenna elements complement each other to improve system reliability. Ideal value should be equal to 10 dB in ideal uncorrelated conditions. A higher DG implies better reception quality. It ensures that even if one antenna receives a weak signal due to fading, the others can compensate, maintaining the link quality. The measured and simulated values of DG are shown in Figure 19. DG and ECC are related and given by [2].

$$DG \approx 10\sqrt{1 - |ECC|^2} \tag{2}$$

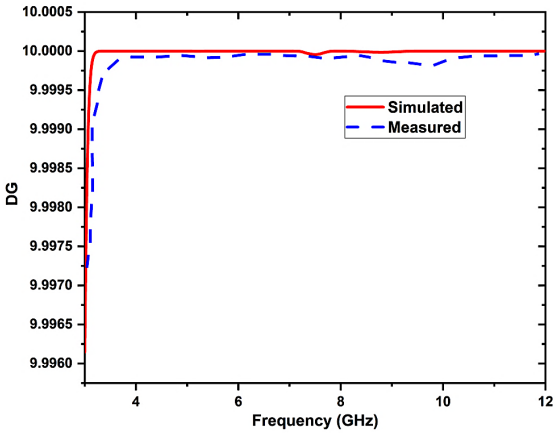

FIGURE 19. DG of the proposed model.

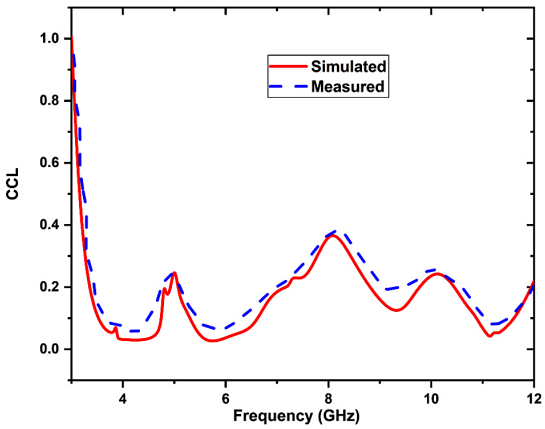

FIGURE 20. CCL of the proposed model.

TABLE 3. Comparison of previous works with the highlighted method.

Ref.	Frequency (GHz)	Substrate	Electrical Dimension	Isolation Technique	S_{12} (dB)	ECC
[4]	2.45	Rogers	$0.89\lambda_0 \times 1.06\lambda_0$	DGS	< -30	-
[6]	24–30	Rogers	$0.42\lambda_0 \times 0.187\lambda_0$	Metamaterial	< -30	0.001
[11]	2.45 and 5.5	Jeans	$0.28\lambda_0 \times 0.375\lambda_0$	-	< -15	-
[12]	4.56–5.65	PET	$0.163\lambda_0 \times 0.245\lambda_0$	Integrated DGS	< -15	< 0.07
[14]	3.6–7	Jeans	$0.326\lambda_0 \times 0.408\lambda_0$	Isolating element and DGS	< -28.5	-
[16]	2.4, 5.2, and 5.8	Jeans	$0.49\lambda_0 \times 0.792\lambda_0$	Isolating element and DGS	< -15	< 0.05
[22]	6.80–8.90	Alumina	$0.49\lambda_0 \times 0.49\lambda_0$	DRA	< -24	-
[23]	16, 25.5, 28 and 32	Rogers	$0.055\lambda_0 \times 0.046\lambda_0$	Isolating element and DGS	< -29.5	< 0.07
[34]	3.1–10.6	FR-4	$0.66\lambda_0 \times 0.47\lambda_0$	Decoupling strips and slotted ground plane	< -15	< 0.02
[35]	3.4–3.6	FR-4	$0.11\lambda_0 \times 0.034\lambda_0$	Side edge layout	< -14.8	< 0.1
[36]	3.4–3.6, 3.6–3.8	FR-4	$1.7\lambda_0 \times 0.91\lambda_0$	Slots	< -20	< 0.01
Pro.	**3–12**	**Polyimide**	$\mathbf{0.294\lambda_0 \times 0.172\lambda_0}$	**Meandered DGS and Inverted U-shaped slots**	$\mathbf{< -25}$	$\mathbf{< 0.0002}$

4.3. CCL

CCL measures the loss in channel capacity due to correlation and MC between MIMO elements. It is a metric derived from S-parameters, and the ideal value of CCL is < 0.5 bits/sec/Hz. In multipath environments, with a high S/N ratio, it is represented by the following Equation (3).

$$C_{\text{loss}} = -\log_2 \det\left(\alpha^R\right)$$

$$\text{where, } \alpha^R = \begin{bmatrix} \alpha_{11} & \cdots & \alpha_{14} \\ \vdots & \ddots & \vdots \\ \alpha_{41} & \cdots & \alpha_{44} \end{bmatrix} \tag{3}$$

$$\alpha_{ii} = 1 - \left(\sum_{j=1}^{N} |S_{ij}|^2\right) \text{ Also } \alpha_{ij} = -\left(S_{ij}^* S_{ij} + S_{ji}^* S_{ij}\right)$$

The measured and simulated values of CCL are maintained at 0.4 bits/s/Hz as shown in Figure 20 for the design.

4.4. TARC

TARC evaluates how effectively the input power is radiated, taking into account both reflections caused by impedance mismatches and mutual coupling between ports. Unlike conventional return loss, TARC incorporates the combined influence of mutual coupling and simultaneous excitation of multiple ports, offering a more realistic measure of performance in MIMO systems. For a two-port MIMO system, it is represented by the following Equation (4).

$$TARC_{ij} = \sqrt{\frac{|S_{ii} + S_{ij}e^{j\theta}|^2 + |S_{ji} + S_{jj}e^{j\theta}|^2}{2}} \tag{4}$$

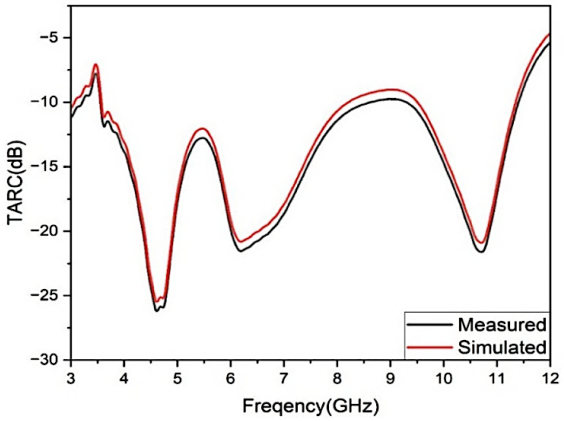

FIGURE 21. TARC: measured and simulated.

The values of TARC (both measured and simulated) are maintained below 10 dB as shown in Figure 21 for the proposed design over the entire operating band. Table 3 presents a comparative analysis of the MIMO antenna with previously reported designs in terms of operating frequency, substrate, dimensions, isolation techniques, S_{12}, and ECC values. It is observed that most of the earlier works employed techniques such as DGS, metamaterials, or isolating elements to enhance isolation, but with larger substrate sizes and limited bandwidth. In contrast, the antenna, fabricated on a compact polyimide of $36 \times 21.1 \times 0.1\,\text{mm}^3$, achieves wideband operation from 3 to 12 GHz with an isolation level more than 25 dB.

5. CONCLUSION

This work has presented a compact, low-profile UWB-MIMO antenna exhibiting wideband operation and enhanced isolation performance, making it well-suited for modern wireless communication systems. The antenna is realized on a polyimide substrate with overall dimensions of $36 \times 21.1 \times 0.1\,\text{mm}^3$ and incorporates a slot-based metamaterial-inspired defected ground structure (DGS) in conjunction with a stub-loaded decoupling network to effectively suppress mutual coupling. The integration of U-shaped stubs, square ring-shaped decoupling elements, and optimized slot configurations enables efficient impedance matching and significant isolation improvement across the operating band. The proposed design achieves $|S_{11}|$ below -10 dB and $|S_{12}|$ better than -25 dB, while maintaining excellent MIMO performance with ECC < 0.0002, DG >9.9 dB, CCL < 0.4 bits/s/Hz, and TARC below -10 dB. Owing to its compact footprint, high isolation characteristics, and robust electrical performance, the suggested antenna is a strong candidate for integration into wireless area networks and multi-standard communication platforms. The combined use of slot-based metamaterial structures and a stub-loaded decoupling network highlights the effectiveness of the suggested approach in achieving wideband operation with superior isolation, offering a practical and scalable solution for next-generation UWB and IoT-enabled wireless systems.

ACKNOWLEDGEMENT

The authors express their sincere gratitude to Universiti Teknikal Malaysia Melaka (UTeM) and the Ministry of Higher Education (MOHE) of Malaysia for their valuable support in funding and facilitating this project. The authors also extend their appreciation to Asia Pacific University of Technology and Innovation (APU), Malaysia for supporting in enhancing and the development of this research.

REFERENCES

[1] Kumar, P., A. K. Singh, R. Kumar, S. K. Mahto, P. Pal, R. Sinha, A. Choubey, and A. J. A. Al-Gburi, "Design and analysis of low profile stepped feedline with dual circular patch MIMO antenna and stub loaded partial ground plane for wireless applications," *Progress In Electromagnetics Research C*, Vol. 140, 135–144, 2024.

[2] Singla, G., R. Sharma, R. Khanna, A. Kumar, and A. J. A. Al-Gburi, "Design of a flexible, highly isolated multiband f-meta MIMO antenna for 5G sub-6 GHz applications using the theory of characteristic modes," *Optik*, Vol. 345, 172632, 2026.

[3] Al-Bawri, S. S., M. T. Islam, T. Shabbir, G. Muhammad, M. S. Islam, and H. Y. Wong, "Hexagonal shaped near zero index (NZI) metamaterial based MIMO antenna for millimeter-wave application," *IEEE Access*, Vol. 8, 181 003–181 013, 2020.

[4] John, D. M., S. Vincent, S. Pathan, and T. Ali, "A compact highly flexible two-element wideband MIMO antenna based on modal analysis for 5G wireless applications," *Physica Scripta*, Vol. 99, No. 7, 075535, 2024.

[5] Fritz-Andrade, E., A. Perez-Miguel, R. Gomez-Villanueva, and H. Jardon-Aguilar, "Characteristic mode analysis applied to reduce the mutual coupling of a four-element patch mimo antenna using a defected ground structure," *IET Microwaves, Antennas & Propagation*, Vol. 14, No. 2, 215–226, 2020.

[6] Devana, V. N. K. R., A. Sowjanya, A. Beno, V. Satyanarayana, B. Kiranmai, N. R. R., L. S. Sai, and B. K. Kumar, "A compact SWB-CSF antenna for millimetre wave wireless applications," *Journal of Infrared, Millimeter, and Terahertz Waves*, Vol. 43, No. 7, 514–526, 2022.

[7] Devana, V. N. K. R., E. K. Kumari, K. S. Chakradhar, P. K. Sharma, D. R. Devi, C. M. Kumar, V. D. Raj, and D. R. Prasad, "A novel foot-shaped elliptically embedded patch-ultra wide band antenna with quadruple band notch characteristics verified by characteristic mode analysis," *International Journal of Communication Systems*, Vol. 35, No. 15, e5284, 2022.

[8] Devana, V. N. K. R. and A. M. Rao, "Design and analysis of dual band-notched uwb antenna using a slot in feed and asymmetrical parasitic stub," *IETE Journal of Research*, Vol. 69, No. 1, 284–294, 2023.

[9] Devana, V. N. K. R., N. Radha, P. Sunitha, F. N. Alsunaydih, F. Alsaleem, and K. Alhassoon, "Compact MIMO UWB antenna integration with Ku band for advanced wireless communication applications," *Heliyon*, Vol. 10, No. 5, e27393, 2024.

[10] Elalaouy, O., M. E. Ghzaoui, and J. Foshi, "A high-isolated wideband two-port MIMO antenna for 5G millimeter-wave applications," *Results in Engineering*, Vol. 23, 102466, 2024.

[11] Sanugomula, M. and K. K. Naik, "A compact high gain circular shaped two-port MIMO antenna with fractal DGS for downlink satellite communication," *Progress In Electromagnetics Research M*, Vol. 125, 135–142, 2024.

[12] Shruthi, B. and K. K. Naik, "Design of enhanced bandwidth of dual element MIMO antenna for wireless applications," *Turkish*

Journal of Computer and Mathematics Education, Vol. 12, No. 6, 1030–1036, 2021.

[13] Raj, G. P. and K. N. Ketavath, "Dual-band inset-fed diamond-shaped patch MIMO antenna for wireless communication applications," *Physica Scripta*, Vol. 99, No. 8, 085546, 2024.

[14] Vanka, S. and C. Chandrasekhar, "A miniaturized-slotted planar MIMO antenna with switchable configuration for dual-/triple-band notches," *AIP Advances*, Vol. 14, No. 2, 025039, 2024.

[15] Saritha, V. and C. Chandrasekhar, "A compact wide band MIMO antenna with quadruple notches in UWB," *Progress In Electromagnetics Research M*, Vol. 108, 237–247, 2022.

[16] Prasad, K. V., T. Haritha, V. S. D. Rekha, B. Alekhya, and V. Saritha, "Isolation improvement of UWB-MIMO design using elliptical stub," *IETE Journal of Research*, Vol. 71, No. 1, 159–170, 2025.

[17] Prasad, K. V. and M. V. Prasad, "Mutual coupling reduction between slotted-T MIMO elements for UWB applications," *Progress In Electromagnetics Research C*, Vol. 107, 203–217, 2021.

[18] Prasad, K. V. and V. S. P. Makkapati, "Investigation of slotted ground and m-shaped DGS in enhancing MIMO antenna isolation," *Wireless Personal Communications*, Vol. 136, No. 4, 2027–2045, 2024.

[19] Nie, L. Y., X. Q. Lin, S. Xiang, B. Wang, L. Xiao, and J. Y. Ye, "High-isolation two-port UWB antenna based on shared structure," *IEEE Transactions on Antennas and Propagation*, Vol. 68, No. 12, 8186–8191, 2020.

[20] Kim, S. and J. Choi, "Two-port UWB MIMO antenna with modified ground for isolation improvement," in *2018 International Symposium on Antennas and Propagation (ISAP)*, 1–2, Busan, Korea (South), 2018.

[21] Sharma, M. K., M. Kumar, and J. P. Saini, "Design and analysis of a compact UWB-MIMO antenna with improved isolation for UWB/WLAN applications," *Wireless Personal Communications*, Vol. 119, No. 4, 2913–2928, 2021.

[22] Urimubenshi, F., D. B. O. Konditi, J. d. D. Iyakaremye, P. M. Mpele, and A. Munyaneza, "A novel approach for low mutual coupling and ultra-compact two port MIMO antenna development for UWB wireless application," *Heliyon*, Vol. 8, No. 3, e09057, 2022.

[23] Kareemulla, S. and V. Kumar, "Diversity performance of band notched ultra-wideband MIMO antenna," *Optik*, Vol. 272, 170128, 2023.

[24] Gómez-Ramírez, P., J. A. Tirado-Méndez, and E. Fritz-Andrade, "Overview of isolation enhancement techniques in MIMO antenna systems," *Electronics*, Vol. 14, No. 22, 4412, Nov. 2025.

[25] Jayaraman, G., I. Singh, and D. K. Choudhary, "Gain and isolation improvement techniques for MIMO antenna: A compendious survey," *Results in Engineering*, Vol. 25, 104482, 2025.

[26] Xing, H., X. Wang, Z. Gao, X. An, H.-x. Zheng, M. Wang, and E. Li, "Efficient isolation of an MIMO antenna using defected ground structure," *Electronics*, Vol. 9, No. 8, 1265, Aug. 2020.

[27] Hassan, K. M. Z., N. Wongkasem, and H. Foltz, "A Ka-band omnidirectional metamaterial-inspired antenna for sensing applications," *Sensors*, Vol. 25, No. 11, 3545, Jun. 2025.

[28] Devadoss, C. P., A. Beno, V. N. K. R. Devana, A. V. Lakshmi, V. L. N. P. Ponnapalli, K. S. Chakradhar, S. C. Sekhar, and P. V. Kumar, "A novel compact MIMO antenna for WiMAX, sub-6 GHz: N77/N78/N79, WLAN and satellite communication applications," *Wireless Networks*, Vol. 32, 131–148, Nov. 2025.

[29] Babu, K. J., R. W. Aldhaheri, L. S. Sai, B. R. Perli, T. Addepalli, S. R. Pasumarthi, B. K. Kumar, and V. N. K. R. Devana, "Design and modal analysis of dual-slot circular patch antenna for ultra-wideband applications," *Journal of Optoelectronics and Advanced Materials*, Vol. 24, No. 7–8, 355–364, 2022.

[30] Devana, V. N. K. R. and A. M. Rao, "A novel compact tri band notched UWB monopole antenna," *Progress In Electromagnetics Research M*, Vol. 91, 123–134, 2020.

[31] Saritha, V., V. N. K. R. Devana, M. B. Lakshmi, M. A. Halimi, G. S. K. G. Devi, N. R. Lavuri, and A. J. A. Al-Gburi, "Low-profile four-port MIMO antenna realizing penta-band notches for UWB systems," *Optik*, Vol. 336, 172454, Sep. 2025.

[32] Devana, V. N. K. R., V. Satyanarayana, A. V. Lakshmi, Y. Sukanya, C. M. Kumar, V. L. N. P. Ponnapalli, and K. J. Babu, "A novel compact fractal UWB antenna with dual band notched characteristics," *Analog Integrated Circuits and Signal Processing*, Vol. 110, No. 2, 349–360, 2022.

[33] Devana, V. N. K. R., P. B. M. Krishna, D. R. Valluri, P. Seepana, C. V. R. Sankar, V. V. R. Karna, and C. Savanam, "A novel compact MIMO-UWB antenna with improved isolation by using parasitic," *Arabian Journal for Science and Engineering*, 1–14, 2025.

[34] Jaglan, N., S. D. Gupta, E. Thakur, D. Kumar, B. K. Kanaujia, and S. Srivastava, "Triple band notched mushroom and uniplanar EBG structures based UWB MIMO/Diversity antenna with enhanced wide band isolation," *AEU — International Journal of Electronics and Communications*, Vol. 90, 36–44, 2018.

[35] Thakur, V., N. Jaglan, and S. D. Gupta, "Side edge printed eight-element compact MIMO antenna array for 5G smartphone applications," *Journal of Electromagnetic Waves and Applications*, Vol. 36, No. 12, 1685–1701, 2022.

[36] Jaglan, N., S. D. Gupta, and M. S. Sharawi, "18 Element massive MIMO/diversity 5G smartphones antenna design for sub-6 GHz LTE bands 42/43 applications," *IEEE Open Journal of Antennas and Propagation*, Vol. 2, 533–545, 2021.